

# Sensitive detection of HO<sub>2</sub> radicals produced in an atmospheric pressure plasma using Faraday rotation cavity ring-down spectroscopy

Cite as: J. Chem. Phys. **151**, 124202 (2019); <https://doi.org/10.1063/1.5119191>

Submitted: 09 July 2019 . Accepted: 10 September 2019 . Published Online: 30 September 2019

 Michele Gianella, Sioned A. Press,  Katherine M. Manfred, Helen C. Norman,  Meez Islam, and  Grant A. D. Ritchie



View Online



Export Citation



CrossMark

## ARTICLES YOU MAY BE INTERESTED IN

[Adaptive strong-field control of vibrational population in NO<sup>2+</sup>](#)

The Journal of Chemical Physics **151**, 124310 (2019); <https://doi.org/10.1063/1.5115504>

[Facile purification of CsPbX<sub>3</sub> \(X = Cl<sup>-</sup>, Br<sup>-</sup>, I<sup>-</sup>\) perovskite nanocrystals](#)

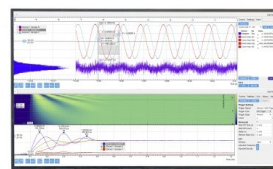
The Journal of Chemical Physics **151**, 121105 (2019); <https://doi.org/10.1063/1.5123306>

[Resonance enhanced two-photon cavity ring-down spectroscopy of vibrational overtone bands: A proposal](#)

The Journal of Chemical Physics **151**, 144201 (2019); <https://doi.org/10.1063/1.5122988>

Challenge us.

What are your needs for  
periodic signal detection?



Zurich  
Instruments



# Sensitive detection of HO<sub>2</sub> radicals produced in an atmospheric pressure plasma using Faraday rotation cavity ring-down spectroscopy

Cite as: J. Chem. Phys. 151, 124202 (2019); doi: 10.1063/1.5119191

Submitted: 9 July 2019 • Accepted: 10 September 2019 •

Published Online: 30 September 2019



Michele Gianella,<sup>1,a)</sup> Sioned A. Press,<sup>1</sup> Katherine M. Manfred,<sup>1,2,b)</sup> Helen C. Norman,<sup>1</sup> Meez Islam,<sup>3</sup> and Grant A. D. Ritchie<sup>1,c)</sup>

## AFFILIATIONS

<sup>1</sup>Department of Chemistry, Physical and Theoretical Chemistry Laboratory, University of Oxford, South Parks Rd., Oxford OX1 3QZ, United Kingdom

<sup>2</sup>Department of Earth Sciences, University of Oxford, South Parks Rd., Oxford OX1 3AN, United Kingdom

<sup>3</sup>School of Science, Engineering and Design, Teesside University, Borough Road, Middlesbrough TS1 3BA, United Kingdom

<sup>a)</sup>Now at: Laboratory for Air Pollution and Environmental Technology, Empa, 8600 Dübendorf, Switzerland.

<sup>b)</sup>Now at: Wolfson Atmospheric Chemistry Laboratories, Department of Chemistry, University of York, York YO10 5DD, United Kingdom.

<sup>c)</sup>Electronic mail: [grant.ritchie@chem.ox.ac.uk](mailto:grant.ritchie@chem.ox.ac.uk)

## ABSTRACT

Cavity ring-down spectroscopy (CRDS) is a well-established, highly sensitive absorption technique whose sensitivity and selectivity for trace radical sensing can be further enhanced by measuring the polarization rotation of the intracavity light by the paramagnetic samples in the presence of a magnetic field. In this paper, we highlight the use of this Faraday rotation cavity ring-down spectroscopy (FR-CRDS) for the detection of HO<sub>2</sub> radicals. In particular, we use a cold atmospheric pressure plasma jet as a highly efficient source of HO<sub>2</sub> radicals and show that FR-CRDS in the near-infrared spectral region (1506 nm) has the potential to be a useful tool for studying radical chemistry. By simultaneously measuring ring-down times of orthogonal linearly polarized light, measurements of Faraday effect-induced rotation angles ( $\theta$ ) and absorption coefficients ( $\alpha$ ) are retrieved from the same data set. The Faraday rotation measurement exhibits better long-term stability and enhanced sensitivity due to its differential nature, whereby highly correlated noise between the two channels and slow drifts cancel out. The bandwidth-normalized sensitivities are  $\alpha_{\min} = 2.2 \times 10^{-11} \text{ cm}^{-1} \text{ Hz}^{-1/2}$  and  $\theta_{\min} = 0.62 \text{ nrad Hz}^{-1/2}$ . The latter corresponds to a minimum detectable (circular) birefringence of  $\Delta n_{\min} = 5 \times 10^{-16} \text{ Hz}^{-1/2}$ . Using the overlapping <sup>9</sup>Q<sub>3</sub>(N = 4–9) transitions of HO<sub>2</sub>, we estimate limits of detection of  $3.1 \times 10^8 \text{ cm}^{-3}$  based on traditional (absorption) CRDS methods and  $6.7 \times 10^7 \text{ cm}^{-3}$  using FR-CRDS detection, where each point of the spectrum was acquired during 2 s. In addition, Verdet constants for pertinent carrier (He, Ar) and bulk (N<sub>2</sub>, O<sub>2</sub>) gases were recorded in this spectral region for the first time. These show good agreement with recent measurements of air and values extrapolated from reported Verdet constants at shorter wavelengths, demonstrating the potential of FR-CRDS for measurements of very weak Faraday effects and providing a quantitative validation to the computed rotation angles.

Published under license by AIP Publishing. <https://doi.org/10.1063/1.5119191>

## I. INTRODUCTION

Radical species are of interest in a broad range of fields including atmospheric chemistry, medicine, and combustion dynamics.<sup>1–7</sup> With regard to this paper, we focus on the hydroperoxyl radical,

HO<sub>2</sub>, which is of particular interest because of its role in the low temperature oxidation chemistry that occurs in both the atmosphere and cold atmospheric pressure plasmas.<sup>8–10</sup> Peroxy radical measurement by chemical amplification (PERCA), chemical ionization mass spectrometry (CIMS), and laser-induced fluorescence assay by gas

expansion (FAGE) are common techniques used to detect HO<sub>2</sub>; however, these all involve reacting HO<sub>2</sub> in a controlled manner and measuring the resultant product species.<sup>11–15</sup> With the development of highly stable and frequency-agile telecom continuous wave (cw) diode laser sources, the near-infrared has been an increasingly popular spectral region in which to detect HO<sub>2</sub> directly. In particular, the 2ν<sub>1</sub> O–H stretching overtone of HO<sub>2</sub> in the 6600–6700 cm<sup>−1</sup> region is well-documented.<sup>16–19</sup> Within this region, there is a strong absorption feature at 6638.20 cm<sup>−1</sup>, which is a superposition of numerous spin-rotation split Q branch transitions, <sup>q</sup>Q<sub>3</sub>(*N*) with *N* = 4–9.<sup>17</sup> The <sup>q</sup>Q<sub>3</sub>(*N* = 4–9) transitions exhibit the strongest absorption cross section in this region and, as Q branch transitions, are attractive for Faraday rotation measurements; in general, optimal transitions for absorption and rotation measurements may be different, and comparisons between the methods should be made at independently optimized transitions and experimental conditions (e.g., pressure). There is also a neighboring feature at 6638.11 cm<sup>−1</sup> which consists of two spin-rotation split P branch transitions, <sup>p</sup>P<sub>0</sub>(6); this second feature has about half the absorption cross section of the <sup>q</sup>Q<sub>3</sub>(*N* = 4–9) absorption and provides a convenient test for calibrating the wavelength and confirming the presence of HO<sub>2</sub>. The rotational fine structure is sufficiently well-resolved (at least at pressure <100 Torr) that cw cavity ring-down spectroscopy (CRDS) can readily be used for the selective and sensitive detection of HO<sub>2</sub>.<sup>20</sup> Onel *et al.* demonstrated a sensitivity of 3.0 × 10<sup>8</sup> cm<sup>−3</sup> for HO<sub>2</sub> at a total sample pressure of 150 mbar using CRDS at 1506 nm.<sup>21</sup>

In the context of radical detection, HO<sub>2</sub> also possesses a nonzero magnetic moment and is therefore susceptible to the Faraday effect, i.e., the polarization of a linearly polarized light wave propagating in the same direction as an applied magnetic field will be rotated when it travels through the paramagnetic sample. The Faraday effect is a consequence of magnetic circular birefringence (MCB) induced by the Zeeman effect, in which left-hand circularly polarized (LHCP) and right-hand circularly polarized (RHCP) waves experience different refractive indices. Since the change in the polarization of light through the medium depends on the concentration of the paramagnetic species as well as the external magnetic field strength, the Faraday effect can be exploited for detection of trace species using a technique called Faraday rotation spectroscopy (FRS).<sup>22–30</sup>

One advantage of Faraday rotation spectroscopy (FRS) is that it is—to some extent—insensitive to potentially interfering diamagnetic compounds such as water and carbon dioxide. Another advantage lies in the noise-suppressing properties of the technique; in the most common configuration, Faraday rotation is measured with a pair of nearly crossed polarizers placed before and after the sample, thus significantly reducing laser intensity noise.<sup>22,28,31–33</sup> Furthermore, flicker noise can be suppressed by shifting the detection of the Faraday rotation signal to frequencies far from zero with field and/or wavelength modulation techniques.<sup>34–36</sup> Several instrument constants—such as amplifier gain and detector responsivity—must be taken into account, however, so obtaining absolute values for the Faraday rotation angle is not trivial.

Faraday rotation spectroscopy can also be combined with optical cavities to increase the sensitivity of the detection of paramagnetic species. Faraday rotation cavity ring-down spectroscopy (FR-CRDS) or polarization-dependent cavity ring-down (PDCRD) was

first demonstrated for molecular oxygen detection using a pulsed laser system at 628 nm and magnetic field of 200 G.<sup>35</sup> Numerous examples of coupling high finesse optical cavities to measure small amounts of Faraday rotation or, more generally, optical rotation exist in the literature.<sup>37–43</sup> Recently, Westberg and Wysocki<sup>34</sup> refined the technique to measure the ring-down times of two orthogonally polarized beams simultaneously to detect molecular oxygen at 762 nm, achieving a polarization rotation sensitivity of 1.3 nrad Hz<sup>−1/2</sup> (per cavity round-trip). One major advantage of this latter implementation is that it puts the Faraday rotation angle on an absolute scale if the ring-down times of two orthogonal, linearly polarized beams are measured. Since the two ring-down times can be measured simultaneously, common mode noise (fluctuations that appear on both polarization channels) cancels out.

In this article, we present a near-infrared FR-CRDS setup consisting of an 86 cm long cavity with ring-down times on the order of 160 μs (finesse  $\mathcal{F} \approx 175\,000$ ) and a DC longitudinal magnetic field of ~700 G over 60 cm. We demonstrate the system by sampling a cold atmospheric pressure plasma (CAPP) and measuring the <sup>q</sup>Q<sub>3</sub>(*N* = 4–9) and <sup>p</sup>P<sub>0</sub>(6) transitions of the 2ν<sub>1</sub> O–H stretch of HO<sub>2</sub> near 6638.20 cm<sup>−1</sup> at a range of sample pressures and magnetic field strengths. Furthermore, we measure known Verdet constants to quantitatively validate our method. This study demonstrates the potential for using FR-CRDS to study the chemistry of atmospheric pressure plasma jets.

## II. THEORY

In this section, we outline the theory associated with the FR-CRDS technique. A complete derivation of the equations presented can be found in the [Appendix](#). In the neighborhood of a transition in a paramagnetic molecule subject to a magnetic field, the Zeeman-splitting of the absorptive and dispersive lineshapes induces magnetic circular dichroism (MCD) and birefringence (MCB). If the magnetic field is applied such that its flux density vector lies in the same direction as the probe beam propagation vector, the transitions with Δ*M<sub>J</sub>* = +1 (Δ*M<sub>J</sub>* = −1) couple to left-hand (right-hand) circularly polarized light, respectively. For a linearly polarized incident wave, circular birefringence leads to a rotation of the plane of polarization by the Faraday rotation angle,<sup>23</sup>

$$\theta = \frac{\pi L_B \Delta n}{\lambda}, \quad (1)$$

where λ is the wavelength of the incident wave, *L<sub>B</sub>* is the field-sample interaction length, and Δ*n* = *n*<sub>+</sub> − *n*<sub>−</sub> is the circular birefringence [*n*<sub>+</sub>: refractive index for a left-hand circularly polarized (LHCP) wave, *n*<sub>−</sub>: refractive index for a right-hand circularly polarized (RHCP) wave], which in turn is dependent on the frequency, on the total gas pressure *p*, on the temperature *T*, on the magnetic field strength *B*, and on the number density of the paramagnetic species [HO<sub>2</sub>].

If a sample with MCB is placed within an optical cavity, birefringence causes the two circular polarizations to possess two slightly different resonance frequencies. We assume that the resonance frequency difference is smaller than the cavity and laser linewidths so that both eigenpolarizations oscillate simultaneously. When the incident wave is abruptly switched off, each eigenpolarization executes

an exponentially damped oscillation with its respective resonance frequency [see (A19)]. A Wollaston prism placed directly after the cavity mixes the two circular components to produce two orthogonal, linearly polarized (*s* and *p*) waves, which are detected by a pair of photodetectors. A beat note then appears in the measured intensity of each linearly polarized wave in addition to the exponential decay [(A26)]. If the period of the beat note is long compared to the decay time, as it usually is, then each of the decays may still be considered approximately exponential but with modified ring-down times (RDTs), which we denote as  $\tau_s$  and  $\tau_p$ .

Another perhaps simpler picture is the following: after the incident wave has been switched off, the birefringence causes the polarization of the transmitted wave to change with time, while the intensity decreases exponentially. In the case of pure MCB, this change is simply a continuous rotation of the polarization vector. With a polarizer placed between the cavity and photodetectors, the measured decay will depend on the evolution of the projection of the transmitted wave's polarization vector on the polarizer transmission axis with time. For example, if the polarization vector rotates toward the polarizer axis, the measured RDT will appear slightly longer, while if it rotates away from the axis, it will appear shorter.

The Faraday rotation angle,  $\theta$ , for a single pass through the cavity is given by (A32),

$$\theta = \frac{L}{4c} \left( \frac{1}{\tau_p} - \frac{1}{\tau_s} \right), \quad (2)$$

where  $L$  is the cavity length (and, in general,  $L_B \leq L$ ). For the interested reader, a derivation of this equation is presented in the Appendix. Alternatively, there are numerous publications in which equivalent relationships can be found, e.g., the work of Engeln *et al.*,<sup>35</sup> Müller *et al.*,<sup>44</sup> Westberg and Wysocki,<sup>34</sup> and Hayden *et al.*<sup>45</sup> We note that some authors define  $\theta$  *per round-trip*, whereas here it is defined *per pass*. One of the benefits of this technique is the cancellation of common mode noise on the two measured ring-down times. The ratio of the uncertainty of the sample's Faraday rotation angle and absorbance scales with the square root of one minus the correlation coefficient between the two ring-down times,  $\rho$ ,<sup>34</sup>

$$\frac{s_\theta}{s_A} \sim \sqrt{1 - \rho}. \quad (3)$$

Highly reflective dielectric mirror coatings are known to exhibit significant (linear) birefringence and polarization-dependent reflectivity (dichroism).<sup>38</sup> With this additional source of anisotropy, the relationship between  $\theta$  on the one hand and  $\tau_s$ ,  $\tau_p$  on the other becomes significantly more complicated. An expression for  $\theta$  under these conditions is beyond the scope of this article and would require knowledge of the orientations of all the relevant axes (fast and slow axes of each mirror, high and low attenuation axes of each mirror), as well as the amounts of birefringence and dichroism present, and their type (linear, circular). We account for mirror effects with an empirical offset, which is discussed in Sec. IV.

### III. EXPERIMENT

#### A. Optical setup

The experimental setup (Fig. 1) consists of a linear cavity formed by two plano-convex dielectric mirrors (Layertec, reflectivity

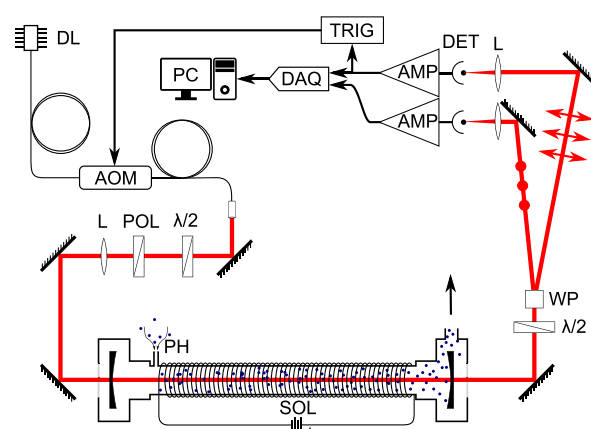


**FIG. 1.** Optical setup. DL: diode laser; AOM: acousto-optic modulator;  $\lambda/2$ : half-wave plate; POL: Glan-Taylor polarizer; L: lens; SOL: solenoid; PH: sampling pinhole; WP: Wollaston prism; DET: detector; AMP: transimpedance amplifier; DAQ: data acquisition module; TRIG: trigger circuitry; and PC: computer running LabVIEW.

$\mathcal{R} \sim 0.99998$ , 1 m radius of curvature). The spacing between the mirror's reflective surfaces is 86 cm. The mirrors are mounted on kinematic mounts (Thorlabs Polaris-K1-2AH) housed within custom stainless steel enclosures. Transparent windows (Thorlabs WG41050-C) are mounted on one face of each enclosure, while on the opposite face, a 0.75 in. UltraTorr fitting (Swagelok SS-12-UT-A-16) connects each enclosure to a 75 cm long borosilicate glass tube (outer diameter: 18 mm). A short tube (6 mm outer diameter, ~15 mm long) allows sampling into the tube at the end opposite the exhaust to the vacuum pump. In normal operation, the plasma jet effluent is directed at a copper pinhole (~0.1 mm diameter) located on the short inlet and the cavity is evacuated through the enclosure at the opposite end of the tube, resulting in the products of the plasma jet being aspirated and drawn through the magnetic field region. The pressure within the cavity is adjusted by varying the rate of evacuation.

The laser source is a cw 1506 nm distributed feedback (DFB) diode laser (NTT NLK1S5GAAA) in a 14-pin, pig-tailed butterfly package (mounted on a Thorlabs LM14S2 mount). The laser diode current and thermoelectric cooler drivers are a LDC 202C and a TED 200C (Thorlabs), respectively. A fiber-coupled acousto-optic modulator (AOM) (Gooch & Housego Fibre-Q), driven by an 80 MHz RF driver (Gooch & Housego A35080), is inserted between the laser diode and the adjustable fiber collimation package (Thorlabs CFC-8X-C). The fiber collimation package is followed by a half-wave plate (Thorlabs WPH05M-1550) and a Glan-Taylor polarizer (Thorlabs GT10-C). The beam emerging from the fiber is elliptically polarized, and so the half-wave plate is used to rotate the ellipse to achieve maximum power transmitted through the Glan-Taylor polarizer. A biconvex lens ( $f = 100$  mm) works in combination with the adjustable collimator to achieve spatial mode-matching of the laser beam to the fundamental transverse cavity mode.

After the cavity, another half-wave plate (Thorlabs WPH05M-1550) is followed by a Wollaston prism (Thorlabs WP10). This half-wave plate is turned in such a way that the *s* and *p*-polarized beams



produced after the Wollaston prism ( $20^\circ$  angular separation) carry equal intensities. The same effect could be achieved by rotating the Wollaston prism, but this would cause the two polarized beams to no longer propagate in the horizontal plane, requiring awkward placement of the detectors. The lens and half-wave plate between the polarizer and Wollaston prism cause no measurable degradation of the linear polarization produced by the Glan-Taylor polarizer. The cavity mirrors, on the other hand, modify the linear polarization into elliptical. We attribute this effect to the linear birefringence of the highly reflective dielectric coating of the mirrors, enhanced by the large finesse of the cavity.<sup>38</sup>

The signals from the two detectors (Thorlabs DET10C) are amplified by a pair of variable gain transimpedance amplifiers (Femto DLPCA-200) with gain bandwidths  $\geq 200$  kHz. The output of one amplifier is sent to a home-built trigger circuit, which switches the RF driver of the AOM off for a predefined duration whenever the detected intensity on the detector exceeds a set threshold. Both amplified detector signals are digitized by a data acquisition module (NI-USB 6356) and processed by a custom LabVIEW (National Instruments) program, which fits the exponential decays, removes outliers, averages, and saves the data to file.

One of the cavity mirrors is mounted on a piezoelectric transducer stage driven by a 150 V driver (Thorlabs TPZ001). The same LabVIEW program responsible for the acquisition modulates the piezoelectric transducer with a user-specified triangular waveform. In standard operation, the piezoelectric transducer is modulated at 150 Hz with an amplitude corresponding to about 10% of the cavity's free spectral range (FSR) and biases the modulation waveform to maintain the timing of the ring-down events approximately in the center of the modulation range. This technique compensates for any slow drift in laser frequency or expansion/contraction of the cavity. For measurements of Verdet constants, the piezoelectric transducer was scanned over  $\sim 1$  FSR at a modulation rate of 30 Hz.

## B. Solenoid

A solenoid with 92 turns was constructed from copper tubing (OD: 6.35 mm, ID: 4.52 mm) coiled with an internal diameter of 19 mm. The copper tube was wrapped in Kapton tape to provide electrical insulation between neighboring turns. This type of construction was selected due to its ease of assembly and cooling. Moreover, the magnetic field can easily be turned on or off and its sense can be reversed. At each end of the solenoid, a segment of about 20 cm of the copper tube was left onto which the electrical and water-cooling connections were affixed. Current to and from the solenoid was carried by two pairs of 1 m-long welding cables (conductive cross section:  $35 \text{ mm}^2$ ). Cooling water was provided by a tap with a normal flow of  $1.25 \text{ l min}^{-1}$ . In operation, the water was heated by  $\sim 15^\circ\text{C}$  for a current of 400 A. The solenoid was supported and held between the two cavity mirror enclosures on the optical bench, and a glass tube (18 mm inner diameter) was inserted along the axis of the solenoid and connected to the cavity mirror enclosures at each end. The power supply unit (PSU; Keysight N8731a) provided up to 400 A of DC current at 8 V. The field magnitude within the solenoid is expected to be 670 G with a current of  $I = 400$  A. The voltage required to drive this current is a modest 4 V, resulting in 1.6 kW dissipated heat.

The longitudinal component of the magnetic field within the solenoid was measured with a Hall effect sensor (Allegro Microsystems A1301) at various points along the axis of the solenoid (which coincides with the beam). The field is reasonably homogeneous over a length of 60 cm with a value of  $694 \pm 15$  G, and, while it falls off quickly close to the solenoid extremities, it does not change the direction. The behavior of the magnetic field at the center with current was determined to be linear, as expected, with a slope of  $1.75 \text{ G A}^{-1}$ . The water-cooled solenoid can be run continuously with a current of 400 A, which is the upper limit of our power supply. Larger fields with higher currents are possible with more powerful power supplies and improved heat management. The DC resistance of the solenoid at room temperature (including all connections and the welding cables) is ca. 10 m $\Omega$ .

## C. Plasma jet source

Two atmospheric pressure plasma jets (APPJs) were used as sources of  $\text{HO}_2$  radicals in this work. The first source consists of a dielectric (glass) tube with two ring electrodes. The discharge is driven by a 10 kV sinusoidal waveform with a frequency of 21.5 kHz. The gas flow was a constant mixture of  $2000 \text{ scm}^3 \text{ min}^{-1}$  of argon and  $100 \text{ scm}^3 \text{ min}^{-1}$  of helium. This type of APPJ is similar to that reported in the work of Alkawareek *et al.*<sup>46</sup> and results in a reproducible transient ( $\mu\text{s}$ ) guided streamer discharge that manifests as a jet with a length of several centimeters emerging from the tube. The second jet is a radio-frequency (rf) plasma source which operates at megahertz frequency with electrodes in a ring-pin configuration. We note that similar devices are commercially available, such as the kIN-Pen, which can be equipped with a gas curtain arrangement, allowing control of the atmosphere surrounding the plume.<sup>47</sup> Details of the ensuing plasma chemistry that is induced in the ambient atmosphere by these sources are not pertinent for this paper other than to note that both are compact, reproducible, and efficient ways of generating  $\text{HO}_2$  radicals.

In both cases, the discharge in the humidified noble gas feed produces excited metastable species and electrons which partially dissociate the water molecules present.  $\text{HO}_2$  is then formed by the reaction of the resulting H atoms with the molecular oxygen in the environment surrounding the plasma. The  $\text{HO}_2$  concentration is highly spatially varied in the effluent, with values exceeding  $10^{13} \text{ cm}^{-3}$ .<sup>48</sup>

## IV. RESULTS AND DISCUSSION

### A. Faraday rotation measurements of $\text{HO}_2$

Figure 2 shows exemplar absorption and Faraday rotation data measured with our FR-CRDS instrument using an rf discharge in humidified Ar surrounded by  $\text{O}_2$  curtain gas to produce  $\text{HO}_2$  radicals. The sample was pulled into the cavity at a rate that maintained a pressure of 30 Torr. Some losses are expected due to the self-reaction of  $\text{HO}_2$  and, possibly, due to the interaction with the glass tube. We have not quantified these losses, but with an estimated residence time of 1 s in the cavity, an initial concentration of  $10^{11} \text{ cm}^{-3}$  would reduce by 26% within 1 s, based on a self-reaction rate of  $1.79 \times 10^{-12} \text{ cm}^3 \text{ s}^{-1}$ .<sup>21</sup> Smaller initial concentrations decrease by less. The magnetic field was set to 694 G. Simultaneous acquisition of the ring-down events on the s and p-polarized arms of the

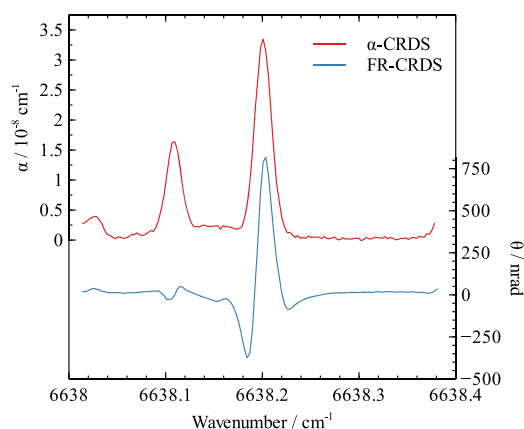


**FIG. 2.** Absorption and Faraday rotation spectra of  $\text{HO}_2$  around  $6638.2\text{ cm}^{-1}$  at 30 Torr ( $B = 694\text{ G}$ ). The spectra cover both the  $^q\text{Q}_3(N = 4-9)$  transitions ( $6638.20\text{ cm}^{-1}$ ) and  $^q\text{P}_0(6)$  transition ( $6638.11\text{ cm}^{-1}$ ).

spectrometer allows for retrieval of absorption coefficient,  $\alpha$ , and  $\theta$  values from the same data set based on (A33) and (2), respectively. Ring-down measurements were acquired across the spectral region with a step size of  $0.0036\text{ cm}^{-1}$  with 200 RDTs averaged (integration time:  $\sim 2\text{ s}$ ) for each spectral data point. For each set of ring-down measurements,  $\tau$  values outside three standard deviations of the mean were removed; typically, these accounted for  $\leq 1\%$  of the measured decays. Note that we have removed the effects of mirror birefringence and background Faraday effect from other gases present, which will be explained in more detail later in this section.

The asymmetry in both the  $\alpha$  and  $\theta$  profiles arises from the multiple overlapping rotational transitions contributing to each feature: the spectra cover both the  $^q\text{Q}_3(N = 4-9)$  transition ( $6638.20\text{ cm}^{-1}$ ) and  $^q\text{P}_0(6)$  transition ( $6638.11\text{ cm}^{-1}$ ). The Q branch transitions exhibit a much stronger Faraday effect than the P branch transition—relative to their comparative absorption cross sections—because the upper and lower states share the same  $g$  factor. This means all subtransitions  $M \leftarrow M - 1$  (and  $M \leftarrow M + 1$ ) are Zeeman-shifted by the same amount and will therefore interfere constructively.

The magnitude of the Faraday rotation angle signal is also dependent on the sample pressure and magnetic field strength. To study the effect of sample pressure, the spectrum of  $\text{HO}_2$  was measured at a fixed magnetic field strength of 694 G, while the total pressure in the cavity was varied between 19 Torr and 55 Torr. The normalized Faraday rotation angle at  $6638.2\text{ cm}^{-1}$  is plotted in Fig. 3 as a function of pressure. As the concentration of  $\text{HO}_2$  varied during the measurement (between  $8.3 \times 10^{10}\text{ cm}^{-3}$  and  $9.8 \times 10^{10}\text{ cm}^{-3}$ ), the measured Faraday rotation angles were normalized to a concentration of  $1\text{ cm}^{-3}$ . For the given magnetic field of 694 G, the maximum Faraday rotation angle is reached at a pressure of 30 Torr. One point (at 35.5 Torr) is not shown because ring-down data near the frequency of maximum rotation were missing. By inspecting the available spectral data for this pressure, it was however clear that the Faraday rotation angle was less than at 30 Torr and more than at 40.4 Torr. The error bars represent the uncertainty in

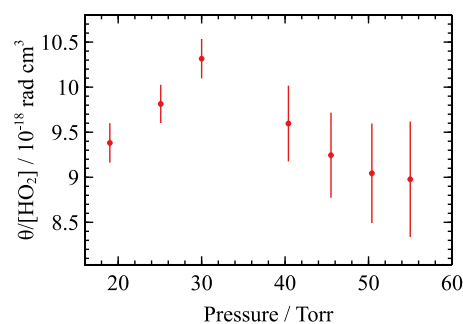


**FIG. 3.** Normalized Faraday rotation angle at  $6638.2\text{ cm}^{-1}$  ( $^q\text{Q}_3$  transitions) as a function of pressure, with  $B = 694\text{ G}$ .

the normalized Faraday rotation angle due to the fluctuations of the ring-down times and to the uncertainty in  $[\text{HO}_2]$  derived from  $\alpha$ . For a fixed volume fraction of  $\text{HO}_2$ , the Faraday rotation angle is known not to be a monotonic function of total pressure.<sup>49</sup> At low pressure, the Zeeman-split subtransitions are Doppler-broadened and are thus relatively easily separated by the Zeeman effect. As the pressure is increased, the overlap between the subtransitions increases (reducing the amount of birefringence per molecule), but since the molecular number density increases proportionally to pressure, the Faraday rotation angle increases. Beyond a certain pressure, which depends on the field strength and on the  $g$ -factors of the upper and lower states of the transition, increasing the pressure further actually decreases the Faraday rotation angle: the increased number density of  $\text{HO}_2$  is not sufficient to compensate for the increasing overlap of the subtransitions.

The Faraday rotation spectrum was then measured at 30 Torr for various values of the magnetic field between 0 G and 694 G (0–400 A solenoid current in steps of 50 A). The normalized Faraday rotation angle at the center of the  $^q\text{Q}_3(N = 4-9)$  feature as a function of magnetic field strength is depicted in Fig. 4. Since the concentration of  $\text{HO}_2$  varied while the measurements were being taken (between  $2.3 \times 10^{10}\text{ cm}^{-3}$  and  $2.9 \times 10^{10}\text{ cm}^{-3}$ ), the data were normalized to a concentration of  $1\text{ cm}^{-3}$ . The vertical error bars represent the uncertainty in the normalized Faraday rotation angle due to the fluctuations of the measured ring-down times and to the uncertainty in  $[\text{HO}_2]$ . The horizontal error bars are due to the

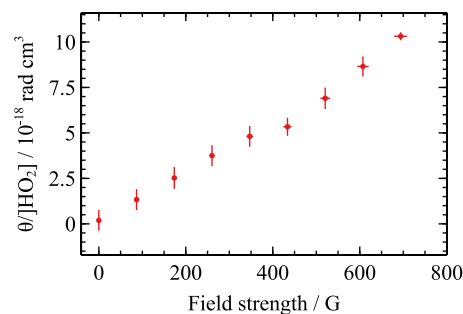


**FIG. 4.** Normalized Faraday rotation angle at  $6638.2\text{ cm}^{-1}$  ( $^q\text{Q}_3$  transitions) as a function of magnetic field strength, with  $p = 30\text{ Torr}$ .

uncertainty in the magnetic field measurement. Within the range of accessible magnetic field strengths, the relationship between Faraday rotation angle and magnetic field is roughly linear. For sufficiently large fields, however, the Faraday rotation angle reaches a maximum at a field strength that is dependent on the sample pressure (see, for example, Fig. 4 in the work of Westberg *et al.*<sup>49</sup> or Fig. 3 in the work of Gianella *et al.*<sup>43</sup>). Figure 4 shows that the maximum is not reached at the field strength of 694 G, meaning that even larger fields could further increase the sensitivity of the spectrometer.

## B. Verdet constant

As mentioned in Sec. IV A, raw data exhibit a nonzero background Faraday rotation angle. We attribute this wavelength-independent offset to two main sources. First, it is well known that interaction of radiation with high reflectivity coatings is polarization dependent; therefore, **s** and **p** polarized light experiences different effective reflectivity.<sup>38</sup> Second, all materials exhibit a very weak Faraday effect, described by the Verdet constant ( $V$ ). Due to the long effective path lengths ( $\sim 10$  km) through the intracavity sample, the main constituent gases of the sample will measurably rotate the polarization of light; in this case, the major constituents are  $N_2$  and  $O_2$  from the ambient air and the carrier gas of the jet (He or Ar). There are very few reports of Verdet constants measured in the near-infrared spectral region partly because the effect is much weaker at these wavelengths compared to the visible. In order to measure pure gases, the plasma jet pinhole inlet was sealed and an inlet on the left-hand enclosure shown in Fig. 1 connected to calibrated gas cylinders via 25 mm OD Teflon tubing. To isolate the influence of mirror birefringence, the Faraday rotation angle was first measured with no applied magnetic field—this value was calibrated daily as it is very sensitive to cavity alignment. Verdet constants were determined in  $O_2$ ,  $N_2$ , Ar, and He—species commonly used in APPJs—by measuring the Faraday rotation angle with a magnetic field of 694 G over the range 6637.715 to 6638.835  $cm^{-1}$  (500 averages per data point, 0.022  $cm^{-1}$  step size) where diamagnetic species show no discernible wavelength dependence of the Faraday rotation angle within the signal-to-noise ratio, SNR, of our instrument (and the wavelength-dependence of the Verdet constant for  $O_2$  is only significant at high partial pressures). A single Verdet constant is therefore reported for each gas across this wavelength region, using the average Faraday rotation angle ( $\bar{\theta}$ ) in the following equation:

$$V = \frac{\bar{\theta}}{pBL_B}, \quad (4)$$

where  $B$  is the magnetic field strength,  $L_B = 60$  cm is the interaction length of the magnetic field, and  $p$  is the pressure of the gas.

Measured Verdet constants are shown in Table I for a range of gases commonly used in feed or curtain gas mixtures for APPJs. Alongside the experimental data, extrapolated Verdet constants are presented for He, Ar,  $O_2$ , and  $N_2$ . The extrapolated values are calculated by assuming  $1/\lambda^2$  dependence of  $V$  and utilizing data from Ingersoll and Leibenberg, Cadène *et al.* and Savukov.<sup>50–52</sup>

Cadène *et al.* measured the Verdet constant of He at 1064 nm using linearly polarized light injected into an optical cavity within

**TABLE I.** Measured Verdet constants of various gases in units of  $nrad\ G^{-1}\ cm^{-1}\ atm^{-1}$ . The second column shows measured values from this work, and these are compared in column three with values extrapolated from published measurements at different wavelengths. The Verdet constant of air was calculated from the values for  $O_2$  and  $N_2$  and excludes water vapor.

Gas	Measured $V$	Extrapolated $V$	References
$O_2$	$0.543 \pm 0.010$	0.676	50
$N_2$	$0.209 \pm 0.005$	0.195	50
Ar	$0.288 \pm 0.006$	0.280	51
He	$0.021 \pm 0.002$	0.019	52
Air (measured)	$0.279 \pm 0.008$		
Air (calculated)	$0.284 \pm 0.015$		

a longitudinal magnetic field.<sup>52</sup> Meanwhile, Ingersoll and Leibenberg's experimental setup utilized a multipass White cell to measure  $V$  for  $N_2$ ,  $D_2$ , and  $O_2$  at a range of wavelengths in the visible region. Similarly to the use of a Wollaston prism in this work, Ingersoll and Leibenberg used a double-image prism to split the beam into two orthogonally polarized components meaning the relative intensity of these can be used to calculate the Faraday rotation angle.<sup>53</sup> Contrastingly, Savukov's work presents noble gas Verdet constants calculated through computer modeling (specifically a particle-hole configuration-interaction method).<sup>51</sup> All extrapolated values presented here show a good level of agreement with the experimentally determined values, with the exception of  $O_2$  whose experimental and predicted value differ significantly. This is not surprising due to the paramagnetic nature of  $O_2$  which results, not only, in a deviation from the inverse-square-wavelength law. Furthermore, the Verdet constant of  $O_2$  is likely to show a greater temperature dependence than other molecules due to its paramagnetic nature.<sup>54</sup> Therefore, a difference in experimental temperature conditions between this work and that of Ingersoll and Leibenberg could further contribute the very different values of experimental and extrapolated  $V$ .

In addition to these extrapolated values, Phelps *et al.* used a single pass, triple modulation setup to directly measure the Verdet constant of air in the near-IR region. Modulation of the magnetic field, light polarization, and light intensity allowed for measurement of values of  $V$  for air at four wavelengths ranging from 632–1550 nm. At 1500 nm, a value of  $(0.27 \pm 0.04) \times 10^{-9}\ rad\ G^{-1}\ cm^{-1}\ atm^{-1}$  was measured,<sup>55</sup> showing close agreement with the values measured here.

There are very few further literature values available for direct measurements of  $V$  in the near-IR due to the fact that Verdet constants in this wavelength region are very small and therefore difficult to measure. The capability to measure Verdet constants of inert gases demonstrates the sensitivity of our spectrometer, while agreement with the sparse literature available in this spectral region provides confidence in the assumptions and approximations applied for the derivation of Eq. (2).

## C. Sensitivity and LOD

In Fig. 2, the  $HO_2$  number density was estimated by fitting a Gaussian lineshape to the  $^9Q_3(N = 4-9)$  absorption feature with the linestrength  $S = 7.1 \times 10^{-21}\ cm^2\ cm^{-1}$ <sup>19</sup> and was found to be

$[\text{HO}_2] = (9.3 \pm 0.1) \times 10^{10} \text{ cm}^{-3}$ . The uncertainty is mainly a consequence of fluctuations in actual  $[\text{HO}_2]$  due to the production and sampling technique rather than noise and so is not representative of the limit of detection. Here, we define the SNR as the ratio between the maximum signal amplitude and the standard deviation of the signal in spectral regions where no absorption (or rotation) occurs:  $\text{SNR}_\alpha = 300$  and  $\text{SNR}_\theta = 1400$ . Each spectral point is the average of 200 ring-down events, corresponding to approximately 2 s integration time. For the experimental settings of Fig. 2, the limits of detection, defined as the concentration needed to produce a spectrum with  $\text{SNR} = 1$ , are  $\text{LOD}_\alpha = [\text{HO}_2]/\text{SNR}_\alpha = 3.1 \times 10^8 \text{ cm}^{-3}$  and  $\text{LOD}_\theta = [\text{HO}_2]/\text{SNR}_\theta = 6.7 \times 10^7 \text{ cm}^{-3}$ . We note that the actual LODs may be lower since if  $[\text{HO}_2]$  is determined through a line-shape fit, thus being a function of several spectral points, the effect of baseline noise on  $[\text{HO}_2]$  would be reduced. Alternatively, one could take “on absorption/off absorption” measurements consisting of only two spectral points (or, for FR-CRDS, switching the sense of the magnetic field); for such measurements, the *signal* would be the differential absorption or Faraday rotation angle, and the *noise* would be the Allan deviation (*vide infra*).

The ring-down times  $\tau_p$  and  $\tau_s$  were measured for 145 min at an average ring-down rate of  $117 \text{ s}^{-1}$  at  $6638.20 \text{ cm}^{-1}$  while sampling a mixture of oxygen and argon through the pinhole at a cavity pressure of 30 Torr (but without any plasma). Figure 5 is an Allan-Werle plot<sup>56</sup> of the absorption coefficient,  $\alpha$ , and of the Faraday rotation angle,  $\theta$ . For integration times of 0.2 s or less, the Allan deviations for both  $\alpha$  and  $\theta$  exhibit white-noiselike behavior; the slopes are  $\alpha_{\min} = 2.2 \times 10^{-11} \text{ cm}^{-1} \text{ Hz}^{1/2}$  and  $\theta_{\min} = 0.62 \text{ nrad Hz}^{1/2}$  (per pass) [or  $1.24 \text{ nrad Hz}^{1/2}$  (per round-trip)]. The latter value is almost identical to the one reported by Westberg and Wysocki<sup>34</sup> at 762 nm. The minimum detectable birefringence,  $\Delta n_{\min}$ , can be derived from Eq. (1) and is

$$\Delta n_{\min} = \frac{\lambda}{\pi L_B} \theta_{\min} = 5 \times 10^{-16} \text{ Hz}^{1/2}. \quad (5)$$

For  $\theta$ , the sensitivity improvement with increasing averaging time continues up to integration times of 60 s, reaching 0.15 nrad, while for  $\alpha$ , there is nothing to be gained from integration longer than 0.5 s, where the sensitivity is  $4 \times 10^{-11} \text{ cm}^{-1}$ . The correlation

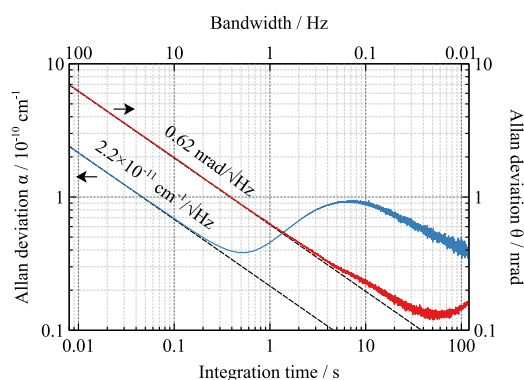


**FIG. 5.** Allan-Werle plot for the absorption coefficient,  $\alpha$ , and the Faraday rotation angle,  $\theta$ .

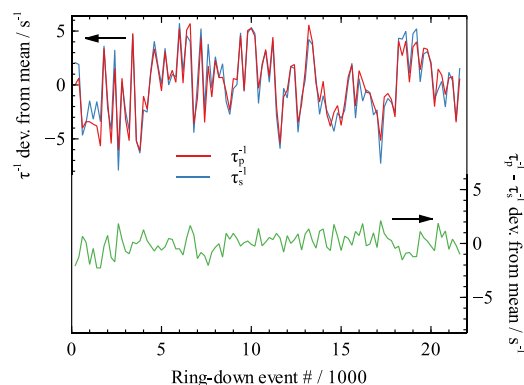


**FIG. 6.** Upper half: deviations of the reciprocal ring-down times,  $\tau_p^{-1}$  and  $\tau_s^{-1}$ , from their respective mean. Lower half: deviation of the difference of the reciprocal ring-down times,  $\tau_p^{-1} - \tau_s^{-1}$ , from the mean. Integration time: 2 s.

coefficient [(3)] was  $\rho = 0.910$  with an integration time of 1 s. This large correlation benefits  $\theta$  but not  $\alpha$  and is the reason for the very different trends in Fig. 5. The plot for  $\alpha$  also indicates the presence of a quasiperiodic fluctuation, which does not affect  $\theta$ , so that we can assume it occurs on both ring-down times and thus cancels out in  $\theta$ . In Fig. 6, a segment of the data used to produce the Allan-Werle plot is shown. The integration time is 2 s, and the correlation between  $\tau_p^{-1}$  and  $\tau_s^{-1}$  is clearly visible in the two upper traces and in the fact that the fluctuations are much reduced in the difference,  $\tau_p^{-1} - \tau_s^{-1}$ . The standard deviations are  $s_{\tau_p^{-1}} = 2.98 \text{ s}^{-1}$  and  $s_{\tau_s^{-1}} = 3.13 \text{ s}^{-1}$  for the two reciprocal ring-down times and  $0.95 \text{ s}^{-1}$  for the difference.

## V. CONCLUSIONS

In this paper, we demonstrate that FR-CRDS is a powerful addition to the spectroscopic toolkit for studying radical species. We used cold atmospheric pressure plasma jets as an efficient source of  $\text{HO}_2$  molecules, an exemplar species of significant importance in both plasma and atmospheric chemistry. Measurements of  $\text{HO}_2$  in the plasma effluent show that FR-CRDS can improve CRDS sensitivity by a factor of five at low pressure (15–60 Torr) with near-infrared (1506 nm) sources. We confirm the robustness of our approach by measuring Verdet constants of  $\text{O}_2$ ,  $\text{N}_2$ , He, and Ar—common principal components found in atmospheric pressure plasma jet systems. In the future, FR-CRDS can be used to study the complex chemistry of these intriguing sources with myriad practical applications.

## ACKNOWLEDGMENTS

The authors would like to acknowledge the UK Engineering and Physical Sciences Research Council (EPSRC; Grant No. EP/P026621/1) and the EU Horizon 2020 FET-OPEN Project ULTRACHIRAL for support. K.M.M. received additional support as the David Cockayne Junior Research Fellow at Linacre College, Oxford.



# APPENDIX: EFFECTS OF DICHROISM AND BIREFRINGENCE ON RING-DOWN MEASUREMENTS

We define the **s** polarization as the vector  $\mathbf{s} = [1, 0]^\top$  and the **p** polarization as  $\mathbf{p} = [0, 1]^\top$ . We assume that the two circular polarizations,  $\mathbf{U}_+$  and  $\mathbf{U}_-$ , are eigenpolarizations of the cavity. This is the case if the anisotropy is given by magnetic circular dichroism and birefringence. If  $\mathbf{J}^{\text{rt}}$  indicates the Jones matrix for a round-trip within the cavity, then  $\mathbf{U}_+$  and  $\mathbf{U}_-$  are its two eigenvectors. The matrix of eigenvectors,

$$\mathbf{U} = [\mathbf{U}_+ \mathbf{U}_-] = \frac{1}{\sqrt{2}} \begin{bmatrix} 1 & 1 \\ +i & -i \end{bmatrix}, \quad (\text{A1})$$

then diagonalizes  $\mathbf{J}^{\text{rt}}$ ,

$$\mathbf{J}^{\text{rt}} = \mathbf{U} \begin{bmatrix} J_+^{\text{rt}} & 0 \\ 0 & J_-^{\text{rt}} \end{bmatrix} \mathbf{U}^\dagger, \quad (\text{A2})$$

where

$$J_\pm^{\text{rt}} = \mathcal{R}e^{-2\kappa_\pm} e^{2i\psi_\pm} \quad (\text{A3})$$

are the complex eigenvalues of  $\mathbf{J}^{\text{rt}}$  written in the polar form, with the polarization-dependent round-trip attenuation,  $\mathcal{R}e^{-2\kappa_\pm}$ , and phase-shift,  $2\psi_\pm$ . It is convenient to introduce the following four parameters:

$$\theta = \frac{\psi_+ - \psi_-}{2} = \frac{\pi\nu}{c} L_B (n_+ - n_-), \quad (\text{A4})$$

$$\tilde{\psi} = \left( \frac{\psi_+ + \psi_-}{2} \right) \bmod 2\pi, \quad (\text{A5})$$

$$\mathcal{D} = \frac{\kappa_+ - \kappa_-}{2} = \frac{\alpha_+ - \alpha_-}{4} L_B, \quad (\text{A6})$$

$$\tilde{\kappa} = \frac{\kappa_+ + \kappa_-}{2} = \frac{\tilde{\alpha}}{2} L. \quad (\text{A7})$$

The parameters  $\theta$  and  $\mathcal{D}$  are measures of birefringence and dichroism, whereas  $\tilde{\psi}$  and  $\tilde{\kappa}$  are the average phase-shift (modulo  $2\pi$ ) and attenuation, respectively. Thus, we can rewrite (A3) as

$$J_\pm^{\text{rt}} = \mathcal{R}e^{-2\tilde{\kappa} \pm 2i\tilde{\psi}} e^{\mp 2\mathcal{D} \pm 2i\theta}. \quad (\text{A8})$$

Consider Fig. 7 which shows a linear cavity into which a plane monochromatic wave is injected. We assume this wave to be abruptly switched off at  $t = 0$ ,

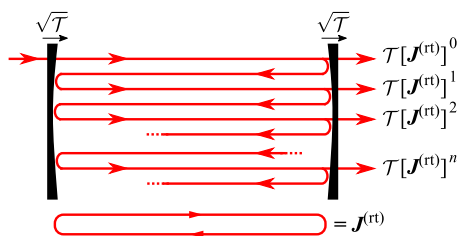


**FIG. 7.** For the derivation of the transmission of a cavity when the input is abruptly switched off.

$$\mathbf{E}_i(t) = \begin{cases} \mathbf{E}_i e^{-2\pi i \nu t}, & t < 0, \\ 0, & t \geq 0. \end{cases} \quad (\text{A9})$$

Before switch off, the cavity transmission is given by the sum (over  $k$ ) of all the partial waves  $\mathcal{T}(\mathbf{J}^{\text{rt}})^k \mathbf{E}_i$ , where we ignore the attenuation and phase-shift of the first pass

$$\mathbf{J}^{\text{cav}} = \mathcal{T} \sum_{k=0}^{\infty} (\mathbf{J}^{\text{rt}})^k = \mathbf{U} \begin{bmatrix} \frac{\mathcal{T}}{1-J_+^{\text{rt}}} & 0 \\ 0 & \frac{\mathcal{T}}{1-J_-^{\text{rt}}} \end{bmatrix} \mathbf{U}^\dagger. \quad (\text{A10})$$

For frequencies  $\nu$  close to a cavity resonance, the eigenvalues  $J_\pm^{\text{cav}} = \mathcal{T}(1 - J_\pm^{\text{rt}})^{-1}$  are (in magnitude) close to unity. Because of anisotropy, however, they are slightly different from one another so that the incident polarization,  $\mathbf{E}_i$ , emerges from the cavity as  $\mathbf{J}^{\text{cav}} \mathbf{E}_i$  which is not parallel to  $\mathbf{E}_i$ . Hence, if the incident polarization is linear, the transmitted polarization will, in general, be elliptical even before switch off. We designate the polarization vector after the cavity before switch off as  $\mathbf{E}'_i$ ,

$$\mathbf{E}'_i = \mathbf{J}^{\text{cav}} \mathbf{E}_i. \quad (\text{A11})$$

After switch off, the partial waves in Fig. 7 vanish one after another every round-trip time. At the time  $t$ , the sum of the partial waves starts at  $k = \lceil t/t^{\text{rt}} \rceil$ . Strictly speaking, the round-trip times for the two circular polarizations are different since the refractive indices are different. However, even for comparatively large values of birefringence, the difference between the “average” round-trip time,  $t^{\text{rt}}$ , and the polarization-specific ones,  $t_\pm^{\text{rt}}$ , is completely negligible. After smoothing the abrupt phase and amplitude jumps by removing the ceiling operator

$$\lceil t/t^{\text{rt}} \rceil \rightarrow \frac{ct}{2L}, \quad (\text{A12})$$

we find with (A2) the transmitted field amplitude,  $\mathbf{E}_f(t)$ , for times  $t \geq 0$ ,

$$\begin{aligned} \mathbf{E}_f(t) &= \mathcal{T} \left[ \sum_{k=ct/2L}^{\infty} (\mathbf{J}^{\text{rt}})^k \right] \mathbf{E}_i e^{-2\pi i \nu t} \\ &= \mathcal{T}(\mathbf{J}^{\text{rt}})^{ct/2L} \left[ \sum_{k=0}^{\infty} (\mathbf{J}^{\text{rt}})^k \right] \mathbf{E}_i e^{-2\pi i \nu t} \\ &= (\mathbf{J}^{\text{rt}})^{ct/2L} \mathbf{J}^{\text{cav}} \mathbf{E}_i e^{-2\pi i \nu t} \\ &= \mathbf{U} \begin{bmatrix} (J_+^{\text{rt}})^{ct/2L} & 0 \\ 0 & (J_-^{\text{rt}})^{ct/2L} \end{bmatrix} \mathbf{U}^\dagger \mathbf{E}'_i e^{-2\pi i \nu t}. \end{aligned} \quad (\text{A13})$$

By inserting (A8) into (A13), we can write  $\mathbf{E}_f$  in the form

$$\mathbf{E}_f(t) = \left( \mathcal{R}e^{ct/2L} e^{(-\tilde{\kappa} + i\tilde{\psi})ct/L} e^{-2\pi i \nu t} \right) \mathbf{U} \begin{bmatrix} (e^{-\mathcal{D} + i\theta})^{ct/L} & 0 \\ 0 & (e^{+\mathcal{D} - i\theta})^{ct/L} \end{bmatrix} \mathbf{U}^\dagger \mathbf{E}'_i. \quad (\text{A14})$$

We then define

$$\frac{1}{2\tau_0} = -\frac{c \ln \mathcal{R}}{2L}, \quad (\text{A15})$$

$$\frac{1}{2\tau} = \frac{1}{2\tau_0} + \frac{c\bar{\kappa}}{L}, \quad (\text{A16})$$

$$\frac{1}{2\tau_{\pm}} = \frac{1}{2\tau} \pm \frac{cD}{L}, \quad (\text{A17})$$

$$\nu_{\pm} = \nu - \frac{c\bar{\psi}}{2\pi L} \mp \frac{c\theta}{2\pi L}, \quad (\text{A18})$$

with which we can write (A14) in the compact form

$$\mathbf{E}_f(t) = \mathbf{U} \begin{bmatrix} e^{-t/2\tau_+ - 2\pi i\nu_+ t} & 0 \\ 0 & e^{-t/2\tau_- - 2\pi i\nu_- t} \end{bmatrix} \mathbf{U}^\dagger \mathbf{E}_i'. \quad (\text{A19})$$

Assuming the polarization,  $\mathbf{E}_i'$ , to be linear and forming a  $\pi/4$  angle with the  $\mathbf{s}$  and  $\mathbf{p}$  axes,  $\mathbf{E}_i' = 2^{-1/2} [1, 1]^\top$ , (A19) becomes

$$\mathbf{E}_f(t) = \frac{e^{-i\pi/4}}{\sqrt{2}} e^{-t/2\tau_+ - 2\pi i\nu_+ t} \mathbf{U}_+ + \frac{e^{i\pi/4}}{\sqrt{2}} e^{-t/2\tau_- - 2\pi i\nu_- t} \mathbf{U}_-, \quad (\text{A20})$$

which is a superposition of two exponentially decaying, circularly polarized waves with two different frequencies and ring-down times. If MCD is negligible, then  $\mathbf{E}_f$  is linear too, but with a different polarization angle.

The Jones matrix for a polarizer with its axis oriented at an angle  $\gamma$  relative to the  $\mathbf{s}$  polarization is the projection matrix

$$\mathbf{P} = \begin{bmatrix} \cos^2 \gamma & \cos \gamma \sin \gamma \\ \cos \gamma \sin \gamma & \sin^2 \gamma \end{bmatrix}. \quad (\text{A21})$$

Its action on the vectors,  $\mathbf{U}_+$ ,  $\mathbf{U}_-$ , yields the two vectors

$$\mathbf{P}\mathbf{U}_{\pm} = \frac{1}{\sqrt{2}} \begin{bmatrix} \cos^2 \gamma & \cos \gamma \sin \gamma \\ \cos \gamma \sin \gamma & \sin^2 \gamma \end{bmatrix} \begin{bmatrix} 1 \\ \pm i \end{bmatrix} \quad (\text{A22})$$

$$= \frac{e^{\pm i\gamma}}{\sqrt{2}} \begin{bmatrix} \cos \gamma \\ \sin \gamma \end{bmatrix}, \quad (\text{A23})$$

both of which point in the fixed direction  $[\cos \gamma, \sin \gamma]^\top$  determined by the axis of the polarizer. If such a polarizer is placed between the cavity output and the detector, the measured irradiance at the detector,  $I(t)$ , is

$$I(t) \propto |\mathbf{E}_{\text{det}}(t)|^2 = |\mathbf{P}\mathbf{E}_f(t)|^2. \quad (\text{A24})$$

The irradiance measured at the detector then follows from (A24) with (A20) and (A23),

$$I(t) \propto e^{-t/\tau_+} + e^{-t/\tau_-} + 2e^{-t/2\tau_+} e^{-t/2\tau_-} \times \cos(-2\pi(\nu_+ - \nu_-)t + 2\gamma - \pi/2). \quad (\text{A25})$$

Finally, using (A17), (A16), and (A18), we can rewrite (A25) as

$$I(t) \propto e^{-t/\tau} [\cosh(2cDt/L) + \sin(2c\theta t/L + 2\gamma)]. \quad (\text{A26})$$

The last equation is a key result and shows that the measured irradiance is an exponential decay with ring-down time  $\tau$  [(A16)], modulated by a factor consisting of

1. a monotonically increasing cosh-term which depends exclusively on the dichroism,  $D$  [(A6)], of the cavity; and
2. an oscillating sin-term with frequency given by the amount of birefringence,  $\theta$  [(A4)], of the cavity.

The oscillating term is a beat note arising from the slightly different resonance frequencies of the two eigenpolarizations which beat against one another during the ring-down event.

For times  $t \ll L/(2cD)$ , we can linearize cosh,

$$\cosh(\mp 2cDt/L) \approx 1. \quad (\text{A27})$$

Similarly, for times  $t \ll L/(2c\theta)$ , we can linearize the sine,

$$\sin\left(\frac{2c\theta}{L}t + 2\gamma\right) \approx \sin(2\gamma) + \frac{2c\theta}{L}t \cos(2\gamma), \quad (\text{A28})$$

and simplify (A26) as

$$\begin{aligned} I(t) &\propto e^{-t/\tau} \left[ 1 + \sin(2\gamma) + \frac{2c\theta t}{L} \cos(2\gamma) \right] \\ &\propto [1 + \sin(2\gamma)] e^{-t/\tau} \left[ 1 + \frac{2c\theta t}{L} \frac{\cos(2\gamma)}{1 + \sin(2\gamma)} \right] \\ &\propto [1 + \sin(2\gamma)] e^{-t/\tau_\gamma}, \quad \gamma \approx 0, \pi/2, \end{aligned} \quad (\text{A29})$$

where

$$\frac{1}{\tau_\gamma} = \frac{1}{\tau} - \frac{2c\theta}{L} \frac{\cos(2\gamma)}{1 + \sin(2\gamma)}, \quad \gamma \approx 0, \pi/2. \quad (\text{A30})$$

Note that the step from the second to the third line of (A29) (i.e., the approximation  $1 + x \approx e^x$ ) implies that  $1 + \sin(2\gamma) \approx 1$  so that (A30) is only valid for  $\gamma \approx 0$  or  $\gamma \approx \pi/2$ . In the present approximation, the observed decay of the irradiance is a single exponential with ring-down time  $\tau_\gamma$ . If the ring-down time is measured with two orthogonal settings of the polarizer, namely,  $\gamma = 0$  ( $\mathbf{s}$  polarization) and  $\gamma = \pi/2$  ( $\mathbf{p}$  polarization), then it follows from (A30) that

$$\begin{aligned} \frac{1}{\tau_p} - \frac{1}{\tau_s} &= \frac{2c\theta}{L} \left[ \frac{\cos(0)}{1 + \sin(0)} - \frac{\cos(\pi)}{1 + \sin(\pi)} \right] \\ &= \frac{4c\theta}{L}, \end{aligned} \quad (\text{A31})$$

or

$$\theta = \frac{L}{4c} \left( \frac{1}{\tau_p} - \frac{1}{\tau_s} \right). \quad (\text{A32})$$

The average absorption coefficient,  $\bar{\alpha}$  (A7), follows from (A16) and (A30),

$$\bar{\alpha} = \frac{1}{2c} \left( \frac{1}{\tau_p} + \frac{1}{\tau_s} - \frac{2}{\tau_0} \right). \quad (\text{A33})$$

The linearization (A28) is only valid for

$$t \ll \frac{L}{2c\theta}. \quad (\text{A34})$$

The exponential prefactor,  $e^{-t/\tau}$ , in (A26) is significant for  $0 \leq t \lesssim 5\tau$  ( $e^{-5} \approx 0.007$ ) so that  $I(t)$  becomes negligible after  $t \approx 5\tau$ , and the time span of interest is  $0 \leq t \leq 5\tau$ . Hence, if  $5\tau \ll L/(2c\theta)$ , then (A34) is fulfilled during the whole ring-down event, and (A32) is valid. Alternatively, if

$$\theta \ll \frac{L}{10c\tau}, \quad (\text{A35})$$

then (A32) is a good approximation. For a cavity with length  $L = 86$  cm and a ring-down time of  $150 \mu\text{s}$ , (A32) is a good approximation only if  $\theta \ll 2 \mu\text{rad}$ . The dynamic range could be extended toward larger birefringences by foregoing the linearizations above and treating the measured decays, which are no longer single exponentials, accordingly.

## REFERENCES

- P. J. Crutzen, "The influence of nitrogen oxides on the atmospheric ozone content," *Q. J. R. Meteorol. Soc.* **96**, 320–325 (1970).
- M. Blocquet, C. Schoemaeker, D. Amedro, O. Herbinet, F. Battin-Leclerc, and C. Fittschen, "Quantification of OH and HO<sub>2</sub> radicals during the low-temperature oxidation of hydrocarbons by fluorescence assay by gas expansion technique," *Proc. Natl. Acad. Sci. U. S. A.* **110**, 20014–20017 (2013).
- J. P. Eiserich, M. Hristova, C. E. Cross, A. D. Jones, B. A. Freeman, B. Halliwell, and A. van der Vliet, "Formation of nitric oxide-derived inflammatory oxidants by myeloperoxidase in neutrophils," *Nature* **391**, 393–397 (1998).
- B. J. Finlayson-Pitts, "Tropospheric air pollution: Ozone, airborne toxics, polycyclic aromatic hydrocarbons, and particles," *Science* **276**, 1045–1051 (1997).
- Y. A. Bakhirkin, A. A. Kosterev, C. Roller, R. F. Curl, and F. K. Tittel, "Mid-infrared quantum cascade laser based off-axis integrated cavity output spectroscopy for biogenic nitric oxide detection," *Appl. Opt.* **43**, 2257–2266 (2004).
- S. M. Cristescu, D. Marchenko, J. Mandon, K. Hebelstrup, G. W. Griffith, L. A. J. Mur, and F. J. M. Harren, "Spectroscopic monitoring of NO traces in plants and human breath: Applications and perspectives," *Appl. Phys. B* **110**, 203–211 (2013).
- F. A. F. Winiberg, S. C. Smith, I. Bejan, C. A. Brumby, T. Ingham, T. L. Malkin, S. C. Orr, D. E. Heard, and P. W. Seakins, "Pressure-dependent calibration of the OH and HO<sub>2</sub> channels of a FAGE HO<sub>2</sub> instrument using the highly instrumented reactor for atmospheric chemistry (HIRAC)," *Atmos. Meas. Tech.* **8**, 523–540 (2015).
- H. Levy, "Normal atmosphere: Large radical and formaldehyde concentrations predicted," *Science* **173**, 141–143 (1971).
- M. Gianella, S. Reuter, A. L. Aguilu, G. A. D. Ritchie, and J.-P. H. van Helden, "Detection of HO<sub>2</sub> in an atmospheric pressure plasma jet using optical feedback cavity-enhanced absorption spectroscopy," *New J. Phys.* **18**, 113027 (2016).
- N. Blin-Simian, S. Pasquiers, and L. Magne, "Removal of formaldehyde by a pulsed dielectric barrier discharge in dry air in the 20 °C to 300 °C temperature range," *J. Phys. D: Appl. Phys.* **49**, 195202 (2016).
- C. A. Cantrell, D. H. Stedman, and G. J. Wendel, "Measurement of atmospheric peroxy radicals by chemical amplification," *Anal. Chem.* **56**, 1496–1502 (1984).
- Y. Liu, R. Morales-Cueto, J. Hargrove, D. Medina, and J. Zhang, "Measurements of peroxy radicals using chemical amplification-cavity ringdown spectroscopy," *Environ. Sci. Technol.* **43**, 7791–7796 (2009).
- D. Amedro, K. Miyazaki, A. Parker, C. Schoemaeker, and C. Fittschen, "Atmospheric and kinetic studies of OH and HO<sub>2</sub> by the FAGE technique," *J. Environ. Sci.* **24**, 78–86 (2012).
- P. S. Stevens, J. H. Mather, and W. H. Brune, "Measurement of tropospheric OH and HO<sub>2</sub> by laser-induced fluorescence at low pressure," *J. Geophys. Res.* **99**, 3543–3557, <https://doi.org/10.1029/93jd03342> (1994).
- G. D. Edwards, C. A. Cantrell, S. Stephens, B. Hill, O. Goyea, R. E. Shetter, R. L. Mauldin, E. Kosciuch, D. J. Tanner, and F. L. Eisele, "Chemical ionization mass spectrometer instrument for the measurement of tropospheric HO<sub>2</sub> and RO<sub>2</sub>," *Anal. Chem.* **75**, 5317–5327 (2003).
- C. A. Taatjes and D. B. Oh, "Time-resolved wavelength modulation spectroscopy measurements of HO<sub>2</sub> kinetics," *Appl. Opt.* **36**, 5817–5821 (1997).
- J. D. DeSain, A. D. Ho, and C. A. Taatjes, "High-resolution diode laser absorption spectroscopy of the O–H stretch overtone band (2,0,0) ← (0,0,0) of the HO<sub>2</sub> radical," *J. Mol. Spectrosc.* **219**, 163–169 (2003).
- L. E. Christensen, M. Okumura, S. P. Sander, R. R. Friedl, C. E. Miller, and J. J. Sloan, "Measurements of the rate constant of HO<sub>2</sub> + NO<sub>2</sub> + N<sub>2</sub> → HO<sub>2</sub>NO<sub>2</sub> + N<sub>2</sub> using near-infrared wavelength-modulation spectroscopy and UV-visible absorption spectroscopy," *J. Phys. Chem. A* **108**, 80–91 (2004).
- J. Thiebaud, S. Crunaire, and C. Fittschen, "Measurements of line strengths in the 2ν<sub>1</sub> band of the HO<sub>2</sub> radical using laser photolysis/continuous wave cavity ring-down spectroscopy (cw-CRDS)," *J. Phys. Chem. A* **111**, 6959–6966 (2007).
- D. Romanini, A. A. Kachanov, N. Sadeghi, and F. Stoeckel, "CW cavity ring down spectroscopy," *Chem. Phys. Lett.* **264**, 316–322 (1997).
- L. Onel, A. Brennan, M. Gianella, G. Ronnie, A. Lawry Aguilu, G. Hancock, L. Whalley, P. W. Seakins, G. A. D. Ritchie, and D. E. Heard, "An intercomparison of HO<sub>2</sub> measurements by fluorescence assay by gas expansion and cavity ring-down spectroscopy within HIRAC (Highly Instrumented Reactor for Atmospheric Chemistry)," *Atmos. Meas. Tech.* **10**, 4877–4894 (2017).
- G. Litfin, C. R. Pollock, R. F. Curl, and F. K. Tittel, "Sensitivity enhancement of laser absorption spectroscopy by magnetic rotation effect," *J. Chem. Phys.* **72**, 6602–6605 (1980).
- I. O. G. Davies, P. E. G. Baird, and J. L. Nicol, "Theory and observation of Faraday rotation obtained with strong light fields," *J. Phys. B: At. Mol. Phys.* **20**, 5371–5386 (1987).
- A. A. Papchenko and E. A. Yukov, "Calculation of Faraday rotation in an atomic gas," *J. Russ. Laser Res.* **15**, 493–504 (1994).
- D. Jacob, M. Vallet, F. Bretenaker, A. Le Floch, and R. Le Naour, "Small Faraday rotation measurement with a Fabry–Pérot cavity," *Appl. Phys. Lett.* **66**, 3546–3548 (1995).
- D. Miyakoshi, M. Aoyama, T. Tohei, A. Minoh, and M. Tsukakoshi, "Saturation effect on the lineshape of Faraday rotation spectrum in krypton," *Jpn. J. Appl. Phys., Part 1* **36**, 7379–7382 (1997).
- S. Aono, "Theory of optical rotation, Faraday effect, and inverse Faraday effect," *Int. J. Quantum Chem.* **75**, 33–45 (1999).
- R. Lewicki, J. H. Doty, R. F. Curl, F. K. Tittel, and G. Wysocki, "Ultrasensitive detection of nitric oxide at 5.33 μm by using external cavity quantum cascade laser-based Faraday rotation spectroscopy," *Proc. Natl. Acad. Sci. U. S. A.* **106**, 12587–12592 (2009).
- P. Kluczyński, S. Lundqvist, J. Westberg, and O. Axner, "Faraday rotation spectrometer with sub-second response time for detection of nitric oxide using a cw DFB quantum cascade laser at 5.33 μm," *Appl. Phys. B* **103**, 451–459 (2011).
- C. Y. Chang and J. T. Shy, "Cavity-enhanced Faraday rotation measurement with auto-balanced photodetection," *Appl. Opt.* **54**, 8526–8530 (2015).
- S. G. So, E. Jeng, and G. Wysocki, "VCSEL based Faraday rotation spectroscopy with a modulated and static magnetic field for trace molecular oxygen detection," *Appl. Phys. B* **102**, 279–291 (2011).
- B. Brumfield, W. Sun, Y. Wang, Y. Ju, and G. Wysocki, "Dual modulation Faraday rotation spectroscopy of HO<sub>2</sub> in a flow reactor," *Opt. Lett.* **39**, 1783–1786 (2014).
- M. Nikodem, D. Weidmann, C. Smith, and G. Wysocki, "Signal-to-noise ratio in chirped laser dispersion spectroscopy," *Opt. Express* **20**, 644–653 (2012).
- J. Westberg and G. Wysocki, "Cavity ring-down Faraday rotation spectroscopy for oxygen detection," *Appl. Phys. B* **123**, 168 (2017).
- R. Engeln, G. Berden, E. van den Berg, and G. Meijer, "Polarization dependent cavity ring down spectroscopy," *J. Chem. Phys.* **107**, 4458–4467 (1997).
- F. K. Tittel and A. A. Kosterev, "Special Issue: Optics: Trends in laser sources, spectroscopic techniques and their applications to trace-gas detection," *Appl. Phys. B* **85**, 171 (2006).
- T. Müller, K. B. Wiberg, and P. H. Vaccaro, "Cavity ring-down polarimetry (CRDP): A new scheme for probing circular birefringence and circular dichroism in the gas phase," *J. Phys. Chem. A* **104**, 5959–5968 (2000).
- H. Huang and K. K. Lehmann, "Effects of linear birefringence and polarization-dependent loss of supermirrors in cavity ring-down spectroscopy," *Appl. Opt.* **47**, 3817 (2008).

- <sup>39</sup>M. Durand, J. Morville, and D. Romanini, "Shot-noise-limited measurement of sub parts-per-trillion birefringence phase shift in a high-finesse cavity," *Phys. Rev. A* **82**, 031803 (2010).
- <sup>40</sup>P. Dupré, "Birefringence-induced frequency beating in high-finesse cavities by continuous-wave cavity ring-down spectroscopy," *Phys. Rev. A* **92**, 053817 (2015).
- <sup>41</sup>A. J. Fleisher, D. A. Long, Q. Liu, and J. T. Hodges, "Precision interferometric measurements of mirror birefringence in high-finesse optical resonators," *Phys. Rev. A* **93**, 013833 (2016).
- <sup>42</sup>F. D. Valle, A. Ejlli, U. Gastaldi, G. Messineo, E. Milotti, R. Pengo, G. Ruoso, and G. Zavattini, "The PVLAS experiment: Measuring vacuum magnetic birefringence and dichroism with a birefringent Fabry-Perot cavity," *Eur. Phys. J. C* **76**, 24 (2016).
- <sup>43</sup>M. Gianella, T. H. P. Pinto, X. Wu, and G. A. D. Ritchie, "Intracavity Faraday modulation spectroscopy (INFAMOS): A tool for radical detection," *J. Chem. Phys.* **147**, 054201 (2017).
- <sup>44</sup>T. Müller, K. B. Wiberg, P. H. Vaccaro, J. R. Cheeseman, and M. J. Frisch, "Cavity ring-down polarimetry (CRDP): Theoretical and experimental characterization," *J. Opt. Soc. Am. B* **19**, 125–141 (2002).
- <sup>45</sup>J. Hayden, J. Westberg, C. L. Patrick, B. Lendl, and G. Wysocki, "Frequency-locked cavity ring-down Faraday rotation spectroscopy," *Opt. Lett.* **43**, 5046–5049 (2018).
- <sup>46</sup>M. Y. Alkawareek, Q. T. Algwari, G. Laverty, S. P. Gorman, W. G. Graham, D. O'Connell, and B. F. Gilmore, "Eradication of *Pseudomonas aeruginosa* biofilms by atmospheric pressure non-thermal plasma," *PLoS One* **7**, 13–15 (2012).
- <sup>47</sup>S. Reuter, J. Winter, A. Schmidt-Bleker, H. Tresp, M. U. Hammer, and K.-D. Weltmann, "Controlling the ambient air affected reactive species composition in the effluent of an argon plasma jet," *IEEE Trans. Plasma Sci.* **40**, 2788–2794 (2012).
- <sup>48</sup>M. Gianella, S. Reuter, S. A. Press, A. Schmidt-Bleker, J. H. Helden, and G. A. Ritchie, "HO<sub>2</sub> reaction kinetics in an atmospheric pressure plasma jet determined by cavity ring-down spectroscopy," *Plasma Sources Sci. Technol.* **27**, 095013 (2018).
- <sup>49</sup>J. Westberg, L. Lathdavong, C. M. Dion, J. Shao, P. Kluczynski, S. Lundqvist, and O. Axner, "Quantitative description of Faraday modulation spectrometry in terms of the integrated linestrength and 1st Fourier coefficients of the modulated lineshape function," *J. Quant. Spectrosc. Radiat. Transfer* **111**, 2415–2433 (2010).
- <sup>50</sup>D. H. Ingersoll and L. R. Leibenberg, "The Faraday effect in gases and vapors I\*," *J. Opt. Soc. Am.* **44**, 566–571 (1954).
- <sup>51</sup>I. M. Savukov, "Particle-hole configuration-interaction polarizabilities and Verdet constants of noble-gas atoms," *Phys. Rev. A* **85**, 1–5 (2012).
- <sup>52</sup>A. Cadène, D. Sordes, P. Berceau, M. Fouché, R. Battesti, and C. Rizzo, "Faraday and Cotton-Mouton effects of helium at  $\lambda=1064$  nm," *Phys. Rev. A* **88**, 1–11 (2013).
- <sup>53</sup>L. R. Ingersoll and W. L. James, "A sensitive photoelectric method for measuring the Faraday effect," *Rev. Sci. Instrum.* **24**, 23–25 (1953).
- <sup>54</sup>L. R. Ingersoll and D. H. Liebenberg, "Faraday effect in gases and vapors III," *J. Opt. Soc. Am.* **48**, 339–343 (1958).
- <sup>55</sup>G. Phelps, J. Abney, M. Broering, and W. Korsch, "A sensitive Faraday rotation setup using triple modulation," *Rev. Sci. Instrum.* **86**, 073107 (2015).
- <sup>56</sup>P. Werle, R. Mücke, and F. Slemr, "The limits of signal averaging in atmospheric trace-gas monitoring by tunable diode-laser absorption-spectroscopy (TDLAS)," *Appl. Phys. B* **57**, 131–139 (1993).